Role of Ce^{4+} in the Scintillation Mechanism of Codoped $Gd_3Ga_3Al_2O_{12}:Ce$

Yuntao Wu,[1,2,3,*] Fang Meng,[1,2] Qi Li,[4,†] Merry Koschan,[1] and Charles L. Melcher[1,2]

[1]*Scintillation Materials Research Center, University of Tennessee, Knoxville, Tennessee 37996, USA*
[2]*Department of Materials Science and Engineering, University of Tennessee, Knoxville, Tennessee 37996, USA*
[3]*Shanghai Institute of Ceramics, Chinese Academy of Sciences, Jiading, Shanghai 201899, People's Republic of China*
[4]*Department of Physics, Wake Forest University, Winston-Salem, North Carolina 27109, USA*

(Received 24 June 2014; revised manuscript received 5 September 2014; published 17 October 2014)

To control the time-response performance of widely used cerium-activated scintillators in cutting-edge medical-imaging devices, such as time-of-flight positron-emission tomography, a comprehensive understanding of the role of Ce valence states, especially stable Ce^{4+}, in the scintillation mechanism is essential. However, despite some progress made recently, an understanding of the physical processes involving Ce^{4+} is still lacking. The aim of this work is to clarify the role of Ce^{4+} in scintillators by studying Ca^{2+} codoped $Gd_3Ga_3Al_2O_{12}:Ce$ (GGAG:Ce). By using a combination of optical absorption spectra and x-ray absorption near-edge spectroscopies, the correlation between Ca^{2+} codoping content and the Ce^{4+} fraction is seen. The energy-level diagrams of Ce^{3+} and Ce^{4+} in the $Gd_3Ga_3Al_2O_{12}$ host are established by using theoretical and experimental methods, which indicate a higher position of the $5d_1$ state of Ce^{4+} in the forbidden gap in comparison to that of Ce^{3+}. Underlying reasons for the decay-time acceleration resulting from Ca^{2+} codoping are revealed, and the physical processes of the Ce^{4+}-emission model are proposed and further demonstrated by temperature-dependent radioluminescence spectra under x-ray excitation.

DOI: 10.1103/PhysRevApplied.2.044009

I. INTRODUCTION

Positron-emission tomography (PET), as a highly sensitive noninvasive medical-imaging technique, is ideally suited for preclinical and clinical imaging of cancer biology, which is important to cancer imaging [1]. Inorganic scintillation crystals, as the key components in PET, are utilized to detect γ rays produced by the annihilation of positrons emitted by injected tracers. The ultimate performance of the PET camera strongly relies on the physical and scintillation properties of the crystals [2]. So far, the single-crystal scintillators for commercial PET cameras are $Bi_4Ge_3O_{12}$ [3], $Lu_2SiO_5:Ce$ (LSO:Ce) [4], and the $Lu_{1.8}Y_{0.2}SiO_5:Ce$ (LYSO:Ce) [5]. Significant improvements have made it possible to add the technology of time of flight (TOF) to improve the image quality of PET [6]. Among the single crystals used for PET applications, LSO:Ce is the best candidate for TOF PET application because of the key parameter of short decay time, e.g., 40 ns for LSO:Ce [4]. One requirement for TOF is the best possible coincidence time resolution (CTR), the figure of merit of which should be 200 ps or better [7]. Since excellent timing resolution can best be achieved on a scintillator with a faster decay time and higher light yield [8], a divalent-ion codoping strategy was applied over the past 6 y to improve the time-response characteristics in trivalent-cation-based oxide scintillators such as LSO:Ce, Ca [9], LYSO:Ce, Ca, LYSO:Ce, Mg [10], and $Lu_3Al_5O_{12}:Ce, Mg$ (LuAG:Ce, Mg) [11,12] without sacrificing (or even enhancing) the light yield when a low codoping concentration of 0.1 at. % is used. Compared with a CTR of 190 ps for LSO:Ce, an even better CTR of 170 ps can be measured on a 0.4 at. % Ca-codoped LSO:Ce single crystal under the same conditions [7] but with a relatively lower light yield. Thus, understanding of the fundamental physical processes causing the acceleration of decay kinetics by divalent codoping is essential for designing other promising candidates for TOF PET application.

There are some hypotheses in the literature for the mechanism of decay-time shortening as a result of codoping. In LSO:Ce, Ca, a proposed cause is the suppression of the slower emission from the sixfold-oxygen-coordinated Ce2 sites and improved chances for migrating charge carriers to be captured by the faster sevenfold-oxygen-coordinated Ce1 sites [13]. It is also ascribed to the reduction of traps acting to slow the scintillation process [14]. Recently, a model of Ce^{4+} ions as an intermediate state in the process leading to a Ce^{3+} excited state was used to explain the decay-time acceleration of LYSO:Ce single crystals by Ca^{2+} or Mg^{2+} codoping [10]. Nevertheless, without solid evidence such as the observation of $(Ce^{3+})^*$

*Corresponding author.
ywu52@utk.edu; caswyt@hotmail.com
†Corresponding author.
liq9@wfu.edu

excitation emission from a scintillator material in which Ce^{4+} has dominating concentration over Ce^{3+}, the Ce^{4+}-emission model is still not firmly proved.

The $Gd_3Ga_3Al_2O_{12}$:Ce (GGAG:Ce) single-crystal scintillator was developed as an improvement of the LuAG:Ce scintillator, based on band-gap engineering [15,16] and cerium valence instability [17] by a Ga^{3+} admixture and energy-level positioning by a Gd^{3+} admixture [18,19]. It shows a very high light yield of up to 50000 photons/MeV, which exceeds by 30%–40% the light-yield value of the best LYSO:Ce scintillators ever reported [20]. A 2-inch-diameter GGAG:Ce single crystal was successfully grown at the Furukawa Co. Ltd. in 2012, which was expected to be a promising candidate for use in PET [21]. However, its main decay component of 88 ns [21], a relatively slow time response compared with LSO:Ce, might be a bottleneck that hinders its application. Our recent work shows that the decay kinetics of GGAG:Ce can be accelerated by codoping with Ca^{2+} ions, though at the expense of light yield [22]. At a certain Ca^{2+} codoping concentration, such as 0.1 at. %, the scintillation decay time can be shortened to about 46 ns with a light yield of about 40000 photons/MeV [23], which may pave the way to its PET and TOF PET applications.

Clarifying the role of a Ca^{2+} codopant in $Gd_3Ga_3Al_2O_{12}$:Ce scintillation kinetics with an eye toward enabling the design of advanced compositions for Ce^{3+}-activated PET and TOF PET applications serves as a motivation for this work. Here we report the correlation between the Ca^{2+} codoping concentration and the ratio between Ce^{3+} and Ce^{4+} as determined by optical absorption spectra and x-ray absorption near-edge spectroscopy (XANES). By varying the Ca^{2+}-codoping concentration, a sample almost completely activated by Ce^{4+} is identified. The related energy-level diagram of Ce^{3+} and Ce^{4+} in the GGAG:Ce host is constructed by using the three-parameter experimental method [24] and the density-functional theory (DFT) + conventional GW (G_0W_0) theoretical calculation method. The higher position of the lowest $5d_1$ excited state of Ce^{4+} in the forbidden gap in comparison to that of Ce^{3+} is confirmed. Furthermore, a Ce^{4+}-emission model is presented and corroborated by temperature-dependent radioluminescence spectra under x-ray excitation. Based on these results, the fundamental origins of the shorter decay time resulting from Ca^{2+} codoping in GGAG:Ce are addressed and compared to the cases of Ca^{2+}- or Mg^{2+}-codoped LSO:Ce, LYSO:Ce, and LuAG:Ce. Experiments on B^{3+} and Ba^{2+}-codoped GGAG:Ce single crystals are also done for comparison.

II. EXPERIMENTAL AND THEORETICAL METHODS

Seven GGAG crystals are grown via the Czochralski method. The compositions are given in Table I. All crystals are grown in inductively heated Ø 60 mm × 60 mm iridium crucibles in a Cyberstar Oxypuller 05-03 Czochralski growth station. Three percent excess Ga is added to an otherwise stoichiometric melt composition in order to compensate for its volatilization loss from the melt. In all cases, the dopant and codopant concentrations given refer to the initial starting melt, and calculations are based on the assumption that the dopants substituted for Gd are based on atomic-size matching. Note that the dopant concentrations in the finished boules will differ from that in the melt due to segregation at the solid-liquid interface. The growth atmosphere is flowing nitrogen with a small fraction of a percent oxygen.

TABLE I. The concentration of activator and codopants in GGAG melt; the concentrations given are with respect to Gd.

Compositions	Ce concentration (at. %)	Codopant concentration (at. %)
GGAG:Ce	0.2	...
GGAG:Ce, Ca	0.2	0.1
	0.2	0.2
	0.2	0.4
GGAG:Ce, Ba	0.2	0.2
GGAG:Ce, B	0.2	0.2

Optical absorption spectra are measured with a Varian Cary 5000 uv-visible NIR spectrophotometer in the 200–800-nm range. Photoluminescence (PL) emission and excitation spectra are measured with a HORIBA Jobin Yvon Fluorolog-3 spectrofluorometer. The excitation light passes through an excitation monochromator with a 1-nm bandpass to ensure monochromaticity. Similarly, the emission monochromator is set at a 1-nm bandpass to select emission light of a specific wavelength. A 450-W continuous xenon lamp is used as the excitation source in emission and excitation spectra.

XANES spectra of codoped GGAG:Ce single crystals are recorded at BL14W1, a wiggler-based beam line in the Shanghai Synchrotron Radiation Facility. Room-temperature measurements are made at the Ce L_{III} edge (5723 eV), in the fluorescence mode due to the low cerium content, by using a Si(111) double-crystal monochromator. The XANES spectra are recorded in two regions: (i) from 5700 to 5720 eV (pre-edge) every 0.5 eV with 5-s accumulation time per point; (ii) from 5720 to 5780 eV (XANES), every 0.5 eV with 8-s accumulation time per point. The powders are evenly coated on transparent tape for measurements. The XANES spectra of Ce^{4+} and Ce^{3+} standard samples are recorded at the x-ray absorption fine structure station of Beijing Synchrotron Radiation Facility, and the specific measurement description can be found in Ref. [25]. All spectra are normalized in the same way by using the ATHENA software [26].

For temperature-dependent radioluminescence spectra, a sample is mounted on a cold finger of the cryostat. The pressure is reduced to 12 mTorr, and the sample is measured from 500 to 40 K to avoid interference from thermoluminescence when irradiated by an x-ray generator (X-ray Model; CMX003) at 35 kV and 0.1 mA.

The absolute light-yield measurement is recorded by using a pulse processing chain consisting of a Hamamatsu R2059 photomultiplier tube (PMT) operated at -1500 V_{bias}, an Ortec 672 amp, a Canberra model 2005 pre-amp, and a Tukan 8 k multichannel analyzer. The PMT is directly coupled to each sample by using mineral oil, and a polytetrafluoroethylene-lined dome-shaped reflector with a 50-mm diameter is used to maximize the collection of light. The photoelectron yield of the samples is calculated by using the single-photoelectron-peak method. Measurements on the samples are made at a gain of 5 with 2 μs shaping time to provide full light integration. The sample is measured for 20 min during its irradiation with a 15 μCi ^{137}Cs source at a distance of about 20 cm. The reproducibility of the light yield is $\pm 5\%$. Scintillation decay times were measured by using an integrated time-correlated single photon counting setup at room temperature.

Electronic structure calculations of bulk GGAG crystals are carried out by using the Vienna *Ab Initio* Simulation Package (VASP) [27,28] with projector-augmented-wave pseudopotentials and generalized gradient approximation exchange-correlation functionals parametrized by Perdew-Burke-Ernzerhof (PBE) [29]. DFT + U on-site potentials [30] are included for Gd 4f orbitals with $U_{\text{eff}} = 6$ eV [31]. Traditional DFT underestimates the band seriously, in general, and hence is not able to make accurate predictions for the relative energy levels [32]. To solve this problem, we employ the hybrid functional PBE0 [33] and *GW* approximation [34] to determine the band gaps and the positions of Ce^{3+} 4f and 5d levels. The crystal structure of the $R_3Al_5O_{12}$ (R = rare earth metal) prototype is body-centered cubic of space group Ia 3d with 160 (80) atoms in the cubic conventional (primitive) cell [35]. Experimental evidence shows that the substitutional Ga_{Al} can occupy both octahedral (16a) and tetrahedral (24d) sites. We perform calculations on both "ordered" GGAG in which the Ga atoms occupy only 24d sites and 160-atom special quasirandom structure (SQS) [36] with a fixed Ga/Al ratio (1:1 on 16a and 2:1 on 24d) [37] to simulate the complex. The Ce levels are simulated by one Ce_{Gd} impurity in the 160-atom cell. The *GW* approximation is applied on top of the generalized gradient approximation with the Hubbard U parameter (GGA + U) wave functions. The Ce^{4+} impurity is simulated by removing one electron from the cell, and a negative background electron density is added to the system. The kinetic cutoff energy is 500 eV. Calculations sampling the γ point only are performed, but the calculations converge within 1 MeV/atom. A self-consistency convergence tolerance of 1×10^{-6} eV is used for all calculations, and the structures are relaxed until all the force components become less than 0.01 eV/Å. The volumes of the lattices are relaxed with the shape of the cells fixed as cubic.

III. RESULTS AND DISCUSSION

A. Phenomenon: Scintillation decay-time shortening after Ca^{2+} codoping

Scintillation decay curves at room temperature are shown in Fig. 1 for GGAG:Ce and Ca^{2+}-codoped GGAG:Ce single crystals. All decay curves are approximated by two exponentials, corresponding to the prompt and delayed radiative recombination at the Ce^{3+} centers [12]. The peak at 370 ns is thought to be an experimental artifact. The decay components determined from a fit of the experimental data to a two-exponential function are listed in Table II for all

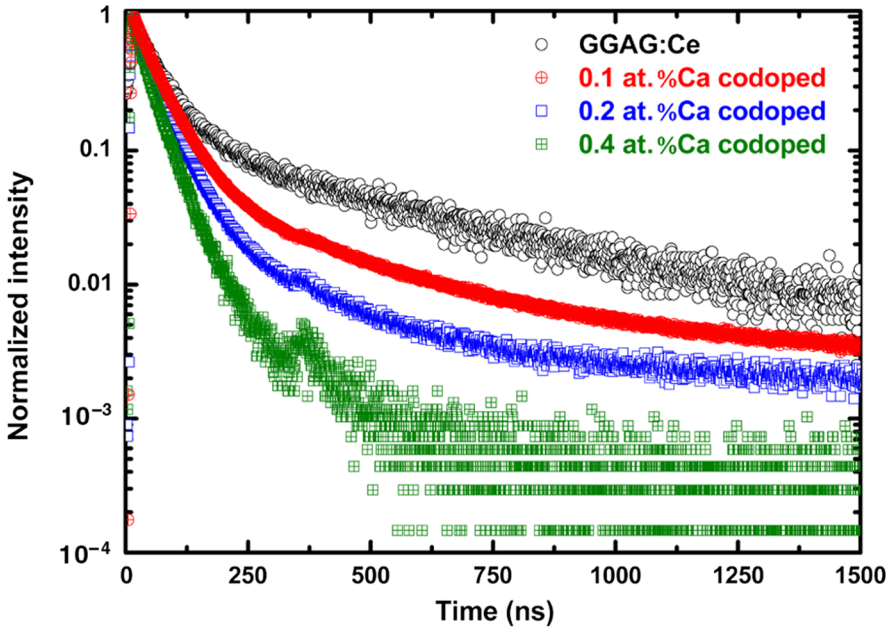

FIG. 1. Scintillation decay profiles of GGAG:Ce and Ca^{2+}-codoped GGAG:Ce single crystals under ^{137}Cs γ-ray source excitation at room temperature.

TABLE II. Scintillation decay-time components of GGAG:Ce doped with different Ca^{2+} concentration and the corresponding percentage of the total scintillation output.

	Decay components	
Compositions	Fast (ns)	Slow (ns)
GGAG:Ce	50 (50%)	372 (50%)
GGAG:Ce, 0.1 at. % Ca	45 (73%)	226 (27%)
GGAG:Ce, 0.2 at. % Ca	40 (78%)	137 (22%)
GGAG:Ce, 0.4 at. % Ca	27 (59%)	59 (41%)

four samples. The most important observation is the continuous shortening with increasing Ca^{2+} concentration of both the prompt and delayed radiative recombination components, similar to the cases of Ca^{2+}-codoped LSO:Ce single crystal [9], Mg^{2+}-codoped LuAG:Ce optical ceramic [11], and single crystal [12]. Specifically, the fast component decreases from 50 ns for the uncodoped sample to 22 ns for the 0.4 at. % Ca-codoped sample, and the slow component in the 0.4 at. % Ca-codoped sample is an order of magnitude faster than the noncodoped sample. However, the decay components in GGAG with Ba^{2+} and B^{3+} codoping become slower than in noncodoped samples [22].

B. Evidence of increased Ce^{4+} percentage

Optical absorption spectra of Ca^{2+}-codoped GGAG:Ce single crystals are plotted in Fig. 2(a) as well as the spectra for B^{3+}- and Ba^{2+}-codoped GGAG:Ce. The $4f \rightarrow 5d_{1,2}$ transitions of Ce^{3+} centered at 340 and 438 nm and the Gd^{3+} $4f \rightarrow 4f$ transition $^8S_{7/2} \rightarrow {}^6I_{3/2}$ at 275 nm [38] can be observed in GGAG:Ce. The B^{3+}- or Ba^{2+}-codoped samples show similar absorption features. Ca^{2+} codoping significantly changes the absorption features. The intensity of the $4f$-$5d_1$ absorption band shows a decreasing trend after Ca^{2+} codoping and almost vanishes when the Ca^{2+}-codoping concentration reaches 0.4 at. %. It implies that the fraction of cerium that is in trivalent form is negligible.

Furthermore, the absorbance of Ca^{2+}-codoped GGAG:Ce increases in the region of 200–370 nm compared to GGAG:Ce. A similar broad absorption band peaking at around 260 nm has been ascribed to the charge-transfer (CT) transition from the O^{2-} levels to the Ce^{3+} ground state in Mg^{2+}-codoped LuAG:Ce [11] and Ca^{2+}-codoped LYSO:Ce [10,39]. The remarkable enhancement of CT absorption intensity with increasing Ca^{2+} concentration indicates an increase in the stable Ce^{4+} fraction, which is consistent with the decreasing intensity of the $4f \rightarrow 5d_1$ absorption of stable Ce^{3+}. The driving force of the formation of Ce^{4+} is the achievement of the charge compensation required when divalent Ca ions locate at trivalent Gd sites. It should be noted that divalent Ba^{2+} codoping does not show the same effect as Ca^{2+} codoping. We assume that this difference is due to a very low concentration of Ba^{2+} in the lattice due to its much larger ionic radius, which is about 142 pm for the octacoordinated site. In comparison, Gd^{3+} is 105.3 pm and Ca^{2+} is 112 pm [40].

Excitation spectra are much more sensitive to a trace presence of the emission center than are absorption spectra. Consequently, one can detect the center existence via emission spectroscopy, even when it is practically invisible in absorption. To determine if Ce^{3+} is present in a 0.4 at. % Ca^{2+}-codoped GGAG:Ce sample, its photoluminescence excitation and emission are measured; the spectra are shown in Fig. 2(b). Under identical measurement conditions, we observe that the Ce^{3+} $4f \rightarrow 5d_{1,2}$ excitation peaks at 340 and 438 nm and the $5d \rightarrow 4f$ emission peak at 550 nm are very weak in 0.4 at. % Ca^{2+}-codoped GGAG compared with GGAG:Ce, and the integrated PL intensity in the Ca^{2+}-codoped sample is at least one order of magnitude lower than that of noncodoped GGAG:Ce. This result indicates that the Ce^{3+} is at a trace level in the 0.4 at. % Ca^{2+}-codoped sample. It is worth mentioning that, when grown under the same conditions, the 0.4 at. % Ca-codoped GGAG:Ce single crystal is a

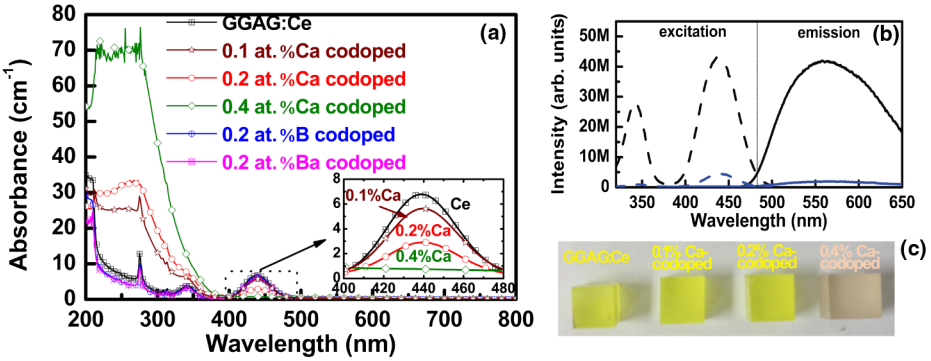

FIG. 2. (a) Optical absorption spectra of GGAG:Ce, GGAG:Ce, B, GGAG:Ce, Ba, and GGAG:Ce, Ca single crystals. The inset is a close-up view for the Ca^{2+}-codoped GGAG:Ce single crystals in the 400–480-nm range; (b) photoluminescence excitation ($\lambda_{em} = 550$ nm) and emission ($\lambda_{ex} = 345$ nm) spectra of GGAG:Ce (black curves) and 0.4 at. % Ca^{2+}-codoped GGAG:Ce (blue curves) single crystals; (c) the Ca^{2+}-codoped GGAG:Ce single-crystal samples.

red-brown color, which is completely different from the yellow color of GGAG:Ce single crystals codoped with other Ca^{2+} concentrations [see Fig. 2(c)].

In order to directly verify the variation of the cerium valence state before and after codoping, XANES is utilized. XANES at the Ce L_{III} edge of GGAG:Ce and 0.4 at. % Ca^{2+}-codoped GGAG:Ce are presented in Fig. 3(a). XANES of B^{3+}- and Ba^{2+}-codoped complexes are also shown. The XANES spectra of Ce^{4+} and Ce^{3+} comparison samples recorded at the Ce L_{III} edge are shown in Fig. 3(b). By comparing the peak shape and the edge position with the reference CeO_2 and CeF_3 samples, the valence states of cerium in these GGAG samples can be determined. Peak *A* is the Ce^{4+} peak with the final state $2p4f^05d^1$, and peak *B* is also a Ce^{4+} peak with the final state of $2p4f^15d^1$. Peak *C* at about 5723 eV is a Ce^{3+} peak, which is associated with the $2p4f^15d$ dipole allowed transition [41]. The XANES data from the GGAG:Ce single crystal indicate that it is a mixture of about 50% Ce^{3+} and 50% Ce^{4+}, as can be seen by comparison with the mixed reference sample. This result is quite different than the pure Ce^{3+} results previously reported for the case of LSO:Ce single crystals [4,42], even though the LSO and GGAG samples are grown in essentially the same growth atmosphere. The XANES data from the 0.4 at. % Ca^{2+}-codoped GGAG:Ce sample show typical Ce^{4+} features. Because of the signal-to-noise limitation, the $I(Ce^{3+})/[I(Ce^{3+})+I(Ce^{4+})]$ ratio cannot be derived by the linear combination fitting method. However, when considering the area under the $4f$-$5d_1$ transition of Ce^{3+} in the Ca-free and 0.4 at. % Ca^{2+}-codoped samples [see Fig. 2(b)], the Ce^{3+} fraction in the 0.4 at. % Ca^{2+}-codoped sample can be estimated to be approximately 4%. Thus, the practical Ce^{3+} concentration in the 0.4 at. % Ca^{2+}-codoped GGAG crystal is roughly estimated to be less than 6 ppmw, given an initial cerium concentration of 458 ppmw, an effective distribution coefficient of 0.322 for cerium ions in GGAG [21], and a Ce^{3+} ratio of 4%. So far, only SiO_2:0.01 mol% Ce sintered in an oxidizing atmosphere has been reported to contain 100% of Ce^{4+} as measured via absorption spectra [43]. Examination of the shoulder corresponding to peak *A* for B^{3+}- or Ba^{2+}-codoped samples reveals an apparent reduction in absorption intensity, consistent with decreasing Ce^{4+} content. This phenomenon is in good agreement with the changes in the CT absorption when compared with the GGAG:Ce. Therefore, the phenomena described above imply a close correlation between scintillation response acceleration and tetravalent cerium concentration increase.

C. Energy-level diagram construction

To shed light on the luminescence behaviors, we construct the energy-level diagrams of Ce^{3+} and Ce^{4+} in GGAG by the three-parameter method based on $E_{4f\text{-}5d1}$ and E_{CT} for Ce^{4+}, $E_{4f\text{-}5d}$ and E_{cd} for Ce^{3+}, and E_g. We present the results from first-principles calculations. The calculated lattice constants and band gaps for $Gd_3Al_5O_{12}$ (GAG), ordered GGAG, and SQS-GGAG are listed in Table III.

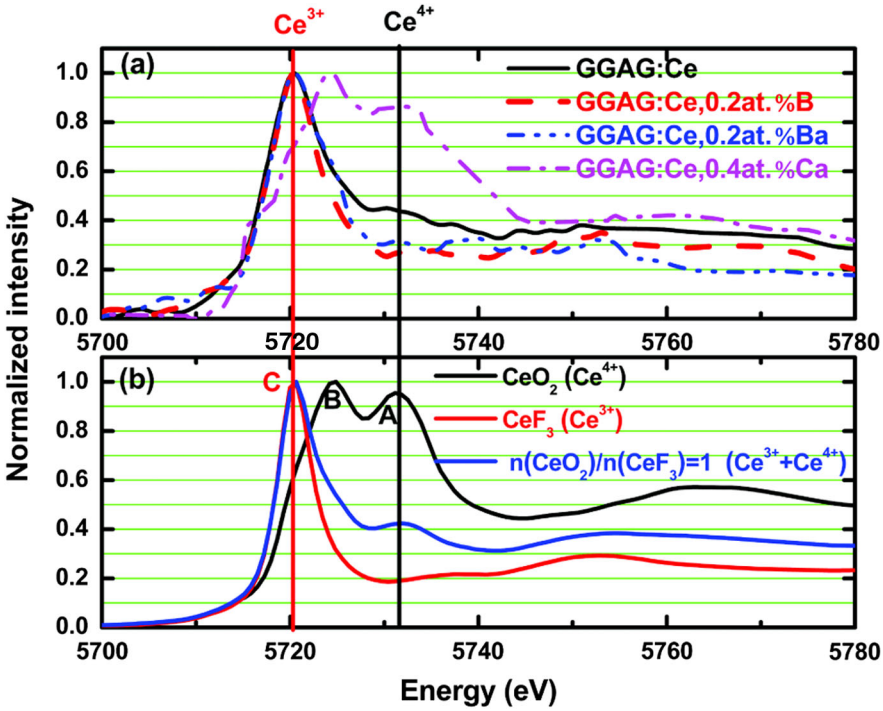

FIG. 3. (a) Ce L_{III}-edge XANES spectra of GGAG:Ce, GGAG:Ce, 0.2 at. % B^{3+}, GGAG:Ce, 0.2 at. % Ba^{2+}, and GGAG:Ce, 0.4 at. % Ca^{2+} single crystals; (b) the XANES spectra of the Ce^{4+} and Ce^{3+} standard samples recorded at the Ce L_{III} edge are used as references.

TABLE III. Calculated lattice constants (a) and band gaps (E_g) of GAG, ordered GGAG, and SQS-GGAG using different functionals.

	GAG		GGAG-ordered		GGAG-SQS	
	a (Å)	E_g (eV)	a (Å)	E_g (eV)	a (Å)	E_g (eV)
GGA + U	12.20	3.96	12.41	3.62	12.40	3.64
PBE0	12.11	7.16	12.30	6.35	12.28	6.40
Expt.	12.11[a]	7.07[b]	...	...	12.27[c]	~6.80

[a]Derived from powder diffraction file for $Gd_3Al_5O_{12}$ (PDF 73-1371).
[b]Derived from Ref. [45].
[c]See Supplemental Material I.

Experimental results are also listed for comparison. Both functionals overestimate the lattice constants. PBE0 predicts a smaller deviation of the lattice constant from the experiment. The SQS structure is predicted to have smaller lattice constants compared to ordered GGAG. Similar results are obtained in Ref. [44]. Accordingly, higher band gaps are predicted for SQS-GGAG. The band gap is significantly reduced (approximately 0.7 eV from PBE0) by Ga doping in the original GAG crystals, consistent with the "band-gap engineering" mechanism in Ref. [16]. Based on the exciton energy (E_{exciton}) for GGAG reported in Ref. [45] and the rule of thumb $E_g = 1.08 \times E_{\text{exciton}}$ [45], E_g is calculated to be 6.8 eV as listed in Table III. Use of the PBE0 functional produces a band gap (6.4 eV) matching the experimental prediction closely.

The partial density of states (PDOS) of SQS-GGAG calculated by GGA + U and PBE0 is shown in Fig. 4. The plot shows the PDOS for two different spin states indicated by positive and negative values. The top of the valance band consists mainly of O $2p$ states, and the conduction band minimum (CBM) consists of Ga $5s$ states. Based on our PBE0 results, there is a significant splitting between the two spin states of the Gd $4f$ orbitals. The first spin state accommodates all seven $4f$ electrons of Gd and is 3.5 eV below the valence band minimum (VBM). The other spin states of Gd $4f$ orbitals are unoccupied, lying at 2.5 eV above the CBM. The CBM Ga $5s$ states calculated by the PBE0 functional shown in Fig. 3 are more localized compared to GGA + U results; however, it is a nonphysical result introduced by insufficient K-mesh sampling. The PDOS results from the PBE0 functional are constructed by using a $2 \times 2 \times 2$ K mesh because of exceedingly high computational complexity when using more refined K-mesh sampling with the PBE0 functional. We perform DFT + G_0W_0 calculations to make the most accurate predictions for the energy levels. The positions of the lowest $4f$ and $5d$ levels of Ce relative to VBM or CBM for Ce^{3+} and Ce^{4+} are shown in Fig. 5(a). The band gap calculated by using G_0W_0 is 6.63 eV, which is even closer to the experimental evaluation compared to PBE0 hybrid functional results (6.40 eV). Both of the lowest $4f$ and $5d$ levels of Ce lie inside the forbidden gap of the host crystal. The $4f \rightarrow 5d_1$ transition energy is quite close, being 2.68 and 2.65 eV, respectively, in Ce^{3+} and Ce^{4+}. A previous *ab initio* calculation based on quantum-cluster approaches predicted the $4f \rightarrow 5d$ transition of 23 927 cm^{-1} (2.97 eV) for Ce_Y,Ga_{Al}^{oct}:YAG systems [46]. By localizing a hole at the Ce_{Gd} site, the lowest Ce $4f$ level becomes unoccupied, and the $4f$-VBM gap increases from 3.13 to 3.60 eV. Correspondingly, the lowest $5d$ level in Ce^{4+} is pushed up toward the CBM, leaving a $5d$ CBM gap of 0.38 eV compared to 0.82 eV in Ce^{3+}. Based on the

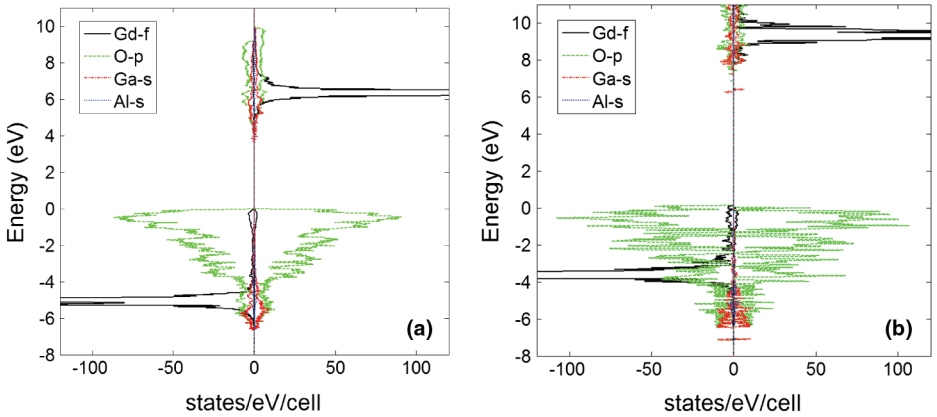

FIG. 4. Calculated partial density of states of 160-atom SQS of GGAG using GGA + U (a) and PBE0 (b) functionals. Positive and negative values represent two different spin states.

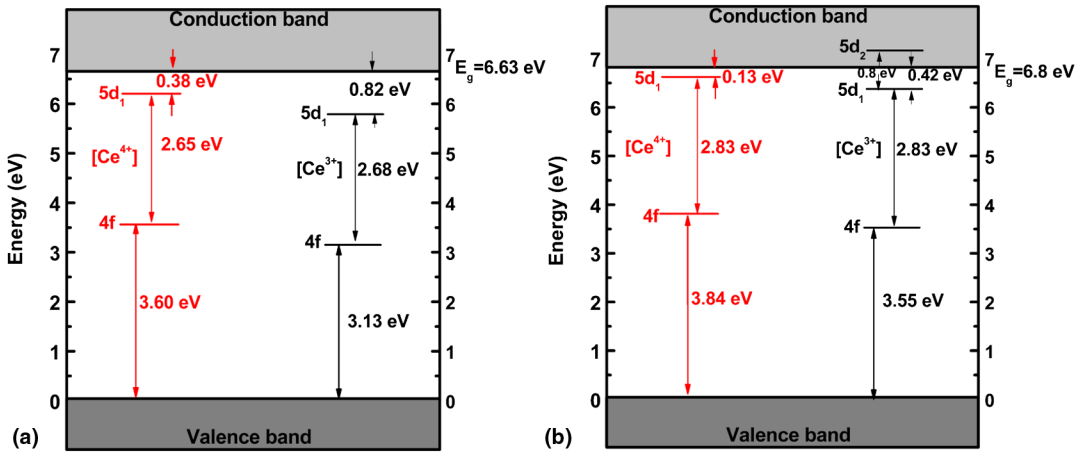

FIG. 5. Schematic energy-level diagrams of Ce^{3+} and Ce^{4+} centers in the GGAG:Ce host: (a) theory (DFT + G_0W_0); (b) experiment (three-parameter method).

calculation results, the theoretical energy-level diagrams of Ce^{3+} and Ce^{4+} are constructed and plotted in Fig. 5(a).

As shown in Fig. 2(a), E_{CT} seems to be within 3.35–3.18 eV (370–390 nm). However, the accurate estimation of the onset of CT absorption of Ce^{4+} (E_{CT}) is influenced by the existence of an additional excitation band between 3.54 and 3.26 eV (350–380 nm) in Ca^{2+}-codoped GGAG:Ce [23]. Based on its fast PL decay time of 3.6 ns and a small Stokes shift of 0.4 eV, along with its correlation with atmosphere annealing, the absorption band is related to F^+ centers (positively charged oxygen vacancies) [23], which is also shown in La^{3+}-doped LuAG single crystals [47] and undoped LuAG single crystals [48]. By analysis of the results of annealing Ca^{2+}-codoped GGAG:Ce in air atmosphere, e.g., 0.2 at. % Ca-codoped GGAG, the influence of the absorption band associated with the F^+ center can be ruled out and the authentic onset of CT absorption of Ce^{4+} can be estimated to be 323 nm (3.84 eV) [22], which shifts to the higher energy side in comparison to the E_{CT} of 3.65 eV (340 nm) for LuAG:Ce, Mg [11] and 3.65–3.54 eV (340–350 nm) for Ca- or Mg-codoped LYSO [10,39]. E_{cd} for Ce^{3+}, the energy separation between the $5d_1$ state of Ce^{3+} and the conduction band, is reported to be 0.42 eV [22]. We recall that the $E_{4f\text{-}5d1}$ for Ce^{3+} is 2.83 eV (438 nm) (see Fig. 2). Under the assumption of a comparable Stokes shift, the $E_{4f\text{-}5d1}$ value for Ce^{4+} is assumed to be the same as that of Ce^{3+} owing to identical radioluminescence emissions (see Fig. 7) [10]. On the basis of the above optical parameters, the experimental energy-level diagrams of Ce^{3+} and Ce^{4+} in a GGAG host are constructed and plotted in Fig. 5(b). The deviation between E_{CT} and E_{Vf} (the energy separation between the top of VB and the $4f$ ground state of Ce^{3+}) is within 0.5 eV, which suggests that the Coulomb interaction between the electron transferred to Ce^{3+} ions and the hole kept at O^{2-} ions does compensate for the relaxation energy of the charge transfer state [24]. It is worth noticing that these energy-level positions are in good agreement with the theoretical calculation results, although slight differences in their absolute values exist. It is apparent that in both diagrams the $4f \rightarrow 5d_1$ transition energies are equal for Ce^{3+} and Ce^{4+}, and the Ce^{4+} $5d_1$ state locates in a higher position in the forbidden gap in comparison to that of Ce^{3+}.

D. Modeling Ce^{4+} emission

To prove that the scintillation occurs from Ce^{4+}, pulse height measurements under ^{137}Cs γ-ray source excitation are made of 0.4 at. % Ca^{2+}-codoped GGAG:Ce, a sample containing negligible Ce^{3+}, and noncodoped GGAG:Ce; results are shown in Fig. 6. By using the data from the radioluminescence spectra, the emission-weighted quantum efficiency of the R2059 PMT is found to be 10% for both samples. The light yield of the 0.4 at. % Ca^{2+}-codoped sample is estimated to be 14800 ± 740 photons/MeV, about one-third of that in GGAG:Ce (44600 ± 2230 photons/MeV). In general, the featured photoluminescence excitation (or absorption) and emission bands of Ce^{3+} can be observed even though its content is at trace levels [49,50], but it is not sufficient to account for all of the measured photons. Therefore, Ce^{4+} ions must play a vital role in the scintillation emission. Sr_2CeO_4 is one of the rare materials in which Ce^{4+} luminescence has been reported, and in this material the emission is assigned to a ligand-to-metal CT transition of Ce^{4+} [51,52]. However, as for 0.4 at. % Ca^{2+}-codoped GGAG:Ce, an almost pure Ce^{4+} sample, Ce^{3+} emission peaks observed under x-ray excitation (see Fig. 7), and a fast decay time in the nanosecond scale under γ-ray excitation (see Fig. 1) indicate that the Ce^{4+}-emission model cannot be assigned to a CT emission but to another physical process through an intermediate Ce^{3+} state. Rotman, Tuller, and Warde [53] reported that, at high Ca^{2+} concentration codoping in garnets, the Ce^{3+} centers

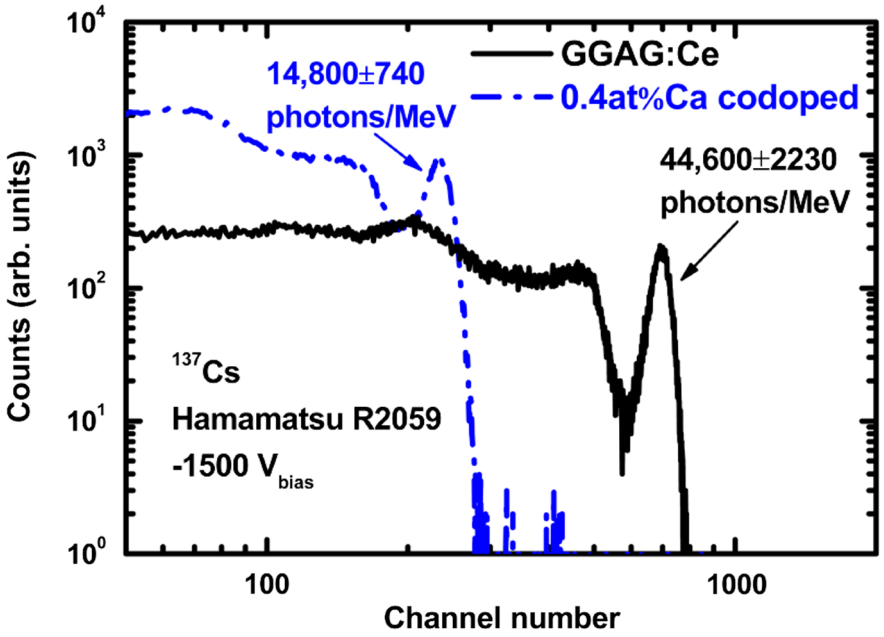

FIG. 6. Pulse height spectra of 662-keV γ ray detected in GGAG:Ce and 0.4 at. % Ca^{2+}-codoped GGAG:Ce single crystals obtained with a Hamamatsu R2059 PMT.

completely converted into stable Ce^{4+} but did show typical Ce^{3+} luminescence under accelerated electron excitation in cathodoluminescence spectra. It was explained by an immediate capture of electrons from the conduction band (CB) by stable Ce^{4+} centers which give rise to the excited Ce^{3+} centers and their typical emission afterwards. Similar models have been recently proposed in silicate and garnet scintillators [10,11].

Since for Ce^{3+} thermal ionization to the conduction band is negligible around room temperature (its onset is indicated at 310 K in Ref. [19]), a difference is expected with Ce^{4+} due to its higher $5d_1$ position in the forbidden gap. In order to further corroborate the applicability of the physical processes of Ce^{4+} emission, the temperature-dependent radioluminescence spectra of GGAG:Ce with approximate 50% Ce^{4+} and 0.4 at. % Ca^{2+}-codoped GGAG:Ce with almost pure Ce^{4+} are acquired, as plotted in Figs. 7(a) and 7(b). The measurements are recorded from 500 to 40 K to avoid interference from thermoluminescence [54]. The Ce^{3+} emission is lower at higher temperatures in both cases, although to differing degrees. The integrated intensities derived from x-ray radioluminescence spectra in the region from 450 to 800 nm as a function of temperature are plotted in Fig. 7(c). The quenching of the 0.4 at. % Ca-codoped sample starts at a lower temperature than that of GGAG:Ce, decreasing by 31% over the 300–40-K range, in comparison to a 6% decrease over the same range for GGAG:Ce. This result is in good agreement with a similar measurement reported by Blahuta *et al.* for LYSO:Ce and Ca^{2+}-codoped LYSO:Ce [10]. The solid curve shown in Fig. 7(c) represents a model calculation used to describe thermal quenching of luminescence. The measured steady-state integrated intensity $I(T)$ can be expressed as

$$I(T) = \frac{I_0}{1 + \Gamma_{\rm nr}/\Gamma_r \exp(-E/kT)}, \qquad (1)$$

where $I(T)$ is the scintillation emission intensity at temperature T, I_0 is the scintillation emission intensity at $T = 0$, and $\Gamma_{\rm nr}$ and Γ_r are the nonradiative and the radiative transition probability, respectivelu. ΔE is the activation energy related to the ionization and/or quenching process, and k is the Boltzmann constant. From a fit to Eq. (1), values of $\Delta E = 296 \pm 27$ MeV for GGAG:Ce and $\Delta E = 206 \pm 7$ MeV for 0.4 at. % Ca^{2+}-codoped GGAG:Ce are obtained. This result is consistent with the concept that the $5d_1$ position of Ce^{4+} is higher than the $5d_1$ position of Ce^{3+} in the GGAG host and both the stable Ce^{3+} and Ce^{4+} ions serve as luminescence centers in the GGAG host, providing the same spectra under ionizing radiation. It is worth noting that these two activation energies could not be regarded as the ΔE for Ce^{3+} and Ce^{4+}, because both Ce^{3+} and Ce^{4+} in these two samples participate in the scintillation process under x-ray irradiation. In other words, the $\Delta E = 296 \pm 27$ MeV for GGAG:Ce should be underestimated for Ce^{3+}, and $\Delta E = 206 \pm 7$ MeV for 0.4 at. % Ca^{2+}-codoped GGAG:Ce should be overestimated for Ce^{4+}. In fact, these two values are indeed between 0.42 eV for Ce^{3+} derived from the temperature-dependent photoluminescence decays (in which only Ce^{3+} ions participate) and the 0.13 eV for Ce^{4+} obtained from the three-parameter method.

According to the physical processes of Ce^{3+} luminescence in scintillators [55], the scintillation process

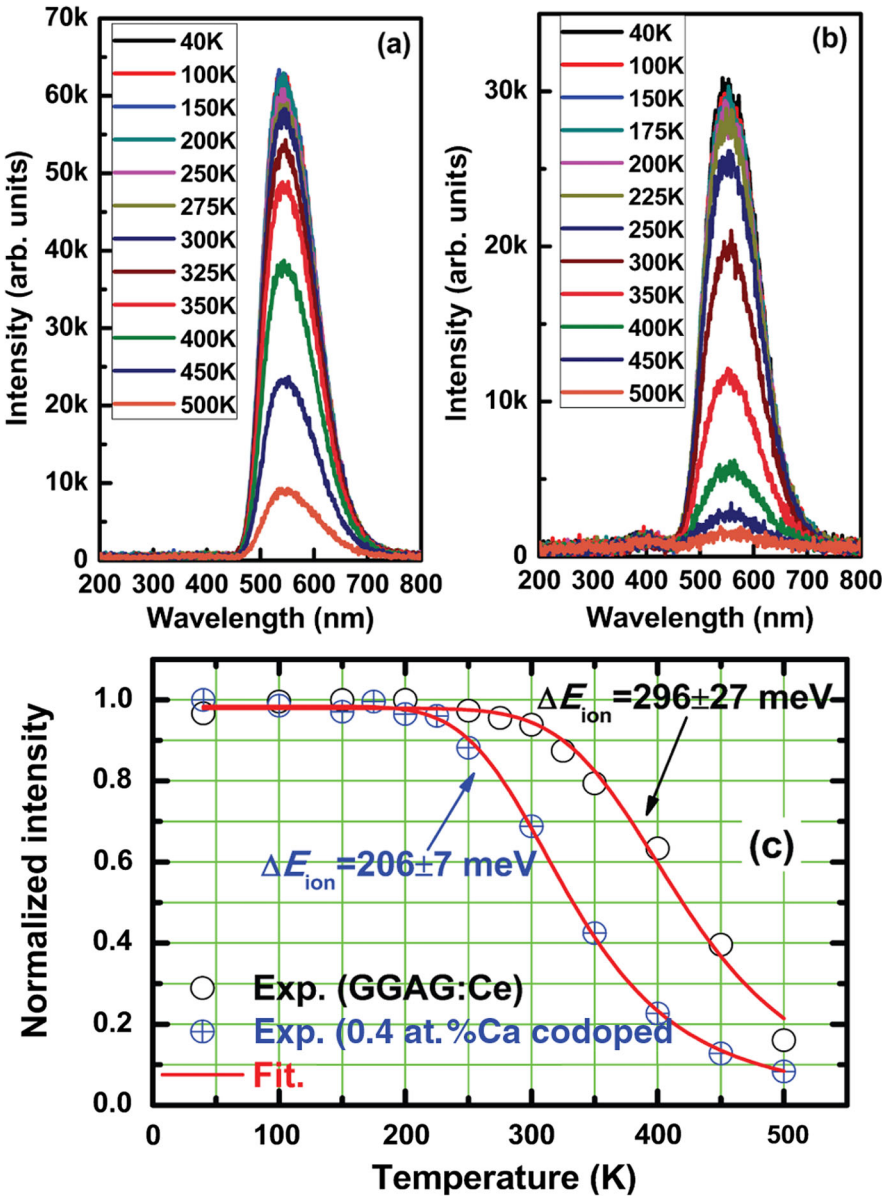

FIG. 7. Temperature-dependent x-ray radioluminescence spectra of GGAG:Ce (a) and 0.4 at. % Ca^{2+}-codoped GGAG:Ce (b). Their intensity variation as a function of temperature is shown in (c), and the red solid lines are fit by following Eq. (1).

involving a stable Ce^{3+} center in the GGAG host should be the creation of initial *e-h* pairs under ionizing irradiation, then a continuous process of capturing a hole from the VB, then capturing an electron from the CB, and finally radiative deexcitation followed by photon emission at around 550 nm:

$$Ce^{3+} + h^{+} \rightarrow Ce^{4+}, \tag{2}$$

$$Ce^{4+} + e^{-} \rightarrow (Ce^{3+})^{*}, \tag{3}$$

$$(Ce^{3+})^{*} \rightarrow Ce^{3+} + h\nu, \tag{4}$$

where h^{+}, e^{-}, $(Ce^{3+})^{*}$, and $h\nu$ represent an electron in the CB, a hole in the VB, an excited Ce^{3+} ion, and the emitted photon, respectively. It is apparent that, in these three processes, the Ce^{4+} acts as an intermediate state. Then, based on the evidence and analysis of Ce^{4+} emission in GGAG:Ce, Ca above, a schematic diagram of the role of stable Ce^{4+} in the scintillation mechanism in GGAG:Ce is developed, as shown in Fig. 8. After irradiation under x ray or γ ray, free charge carriers (*e-h* pairs) are produced in the CB and VB (step 1); a stable Ce^{4+} ion then captures an excited electron from the CB in the empty 5*d* energy levels, and the formation of an excited $(Ce^{3+})^{*}$ center occurs (step 2); the Ce^{3+} emission occurs by radiative deexcitation that leaves the center in the ground state of Ce^{3+} (step 3);

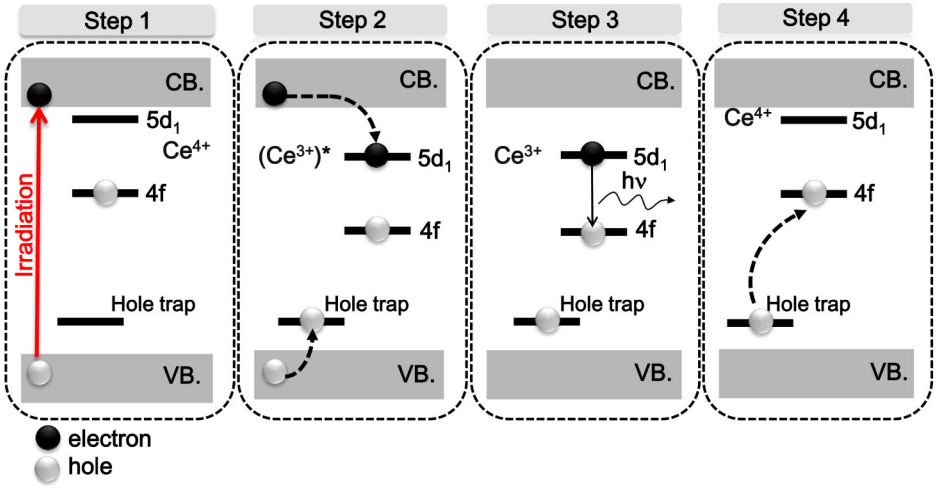

FIG. 8. Schematic diagram of the role of stable Ce^{4+} in the scintillation mechanism in GGAG:Ce.

stable Ce^{4+} is recreated by a hole capture from the valence band or a nearby hole trap (step 4). According to Ref. [52], where Ca^{2+} is introduced into a garnet system, the VB hole can be trapped at neighboring oxygen ligands so that the Ce^{3+} center in the ground state (after step 3) can thus trap a hole localized near the Ca^{2+} ion or a hole from the VB.

The underlying reasons for decay-time shortening by Ca^{2+} codoping in GGAG:Ce could be related to two factors: (i) a much faster emission based on stable Ce^{4+}, which is made possible by bypassing the first step of the stable Ce^{3+} scintillation mechanism under ionization irradiation, i.e., capturing a hole from the VB, and a faster radiative deexcitation of the electron captured at the $5d_1$ state of Ce^{4+} because its E_{cd} is narrower than that of stable Ce^{3+}; (ii) a more efficient energy migration of free charge carriers to activators due to the reduction in the number of shallow traps [22]. The deterioration of the light yield after Ca^{2+} codoping could be related to two factors: (i) the negative consequence of the smaller E_{cd} of Ce^{4+} and (ii) formation of deep traps corresponding to the TL peaks over 300 K [22].

E. Applicability of the Ce^{4+}-emission model

As a practical demonstration, the Ce^{4+}-emission model is applied to explain the improvement of scintillation performance in LSO:Ce, Ca [9], LYSO:Ce, Ca/Mg [10], and LuAG:Ce, Mg [11]. For the case of LuAG:Ce, Mg, the forbidden gap in LuAG is about 7.5–8.0 eV [56,57], the onset of CT is at about 3.75–3.65 eV (330–340 nm), and $E_{4f\text{-}5d1}$ is 2.79 eV (445 nm) [11]. Then, $5d_1$ should be at about 6.5 eV above the VB edge, which means 1–1.5 eV below the CB edge, which fits the fact that the $5d_2$ level in YAG is found at about 0.5 eV below the CB edge [58]. The TL intensity of annealed Mg^{2+}-codoped LuAG:Ce is significantly reduced in comparison to that of annealed LuAG:Ce, without the formation of new TL peaks [11]. Thus, after Mg^{2+} codoping in LuAG:Ce, not only is the decay time accelerated by the formation of Ce^{4+}, but a combination of sufficient separation between the $5d_1$ state of Ce^{4+} and the CB (1–1.5 eV) and trap suppression both contributed to the light-yield enhancement.

Because of the similarity between codoped LSO:Ce and codoped LYSO:Ce, either optical or scintillation properties [9,12,59,60], codoped LYSO:Ce is chosen to be discussed. By using previous reports on LYSO:Ce as an example, based on an E_g of 7.4 eV, an $E_{4f\text{-}5d1}$ of 3.47 eV, and an E_{CT} between 3.54 and 3.65 eV [10], the $5d_1$ state position of Ce^{4+} is 0.28–0.39 eV below the CB. It located at a higher position in the forbidden gap than the $5d_1$ of Ce^{3+} ($\Delta E_{ion} = 0.435$ eV) in LYSO:Ce [61]. Thus, the formation of Ce^{4+} will result in unwanted thermal ionization effects in LYSO:Ce, Ca. Thanks to the TL intensity reduction throughout the measured temperature range in Ca^{2+}-codoped LYSO:Ce [14,60], trap suppression and more efficient energy migration of free charge carriers to activators can be ensured, which in turn favors light-yield enhancement and decay-time shortening. Thus, the time-response optimization in Ce^{3+}-based scintillators for PET and TOF PET applications can be achieved by composition engineering through codoping ions with a lower valence state and closer ionic radius with respect to the substituted cations in matrix in order to increase the stable Ce^{4+} fraction, although at the risk of light-yield deterioration.

IV. SUMMARY

A correlation between the stable Ce^{4+} fraction and the Ca^{2+} codoping concentration is established, and we show that the fraction of the cerium that is in the stable Ce^{3+} state is negligible in GGAG:Ce codoped with 0.4 at. % Ca^{2+}. A higher position of the lowest $5d_1$ excitation state of Ce^{4+} in the forbidden gap in comparison to that of Ce^{3+} is confirmed. A Ce^{4+} emission model at the nanosecond scale under high-energy excitation is given through an intermediate Ce^{3+} state by capturing an electron from the CB,

radiative deexcitation of Ce^{3+}, and a return to the initial state by capturing a hole from a nearby hole trap or the valence band. The underlying reasons for the decay-time shortening by Ca^{2+} codoping in GGAG:Ce are related to a much faster emission from Ce^{4+} in comparison to Ce^{3+} and more efficient and faster energy migration of free charge carriers to activators. The deterioration of the light yield after Ca^{2+} codoping in GGAG:Ce is ascribed to the negative consequence of narrowed E_{cd} for Ce^{4+} and the formation of deep traps after Ca^{2+} codoping. An understanding of the Ce^{4+}-emission model is essential for the composition engineering of the Ce^{3+}-activated scintillators with a fast timing response needed for PET and TOF PET applications. More comprehensive studies are presently under way in which other material systems will be studied.

ACKNOWLEDGMENTS

The authors thank the Shanghai Synchrotron Radiation Facility for the use of beam time at the BL14W1 beam line. The authors gratefully acknowledge the support from Siemens Medical Solutions Molecular Imaging and that offered in part by the National Nature Science Foundation of China (Grant No. 51202276), Shanghai Institute of Ceramics Innovation Program (Grant No. Y39ZC2130G), and Open Fund of the State Key Laboratory of Crystal Material (Grant No. KF1305). Q. L. acknowledges the National Nuclear Security Administration, DNN R&D, through subcontract to Lawrence Berkeley National Laboratory No. DE-AC02-05CH1123, and the U.S. Department of Homeland Security, DNDO, under Contract No. NSF ECCS-1348361.

[1] S. S. Gambhir, Molecular imaging of cancer with positron emission tomography, Nat. Rev. Cancer **2**, 683 (2002).

[2] C. L. Melcher, Scintillation crystals for PET, J. Nucl. Med. **41**, 1051 (2000), http://jnm.snmjournals.org/content/41/6/1051.

[3] M. J. Weber and R. R. Monchamp, Luminescence of $Bi_4Ge_3O_{12}$-spectral and decay properties, J. Appl. Phys. **44**, 5495 (1973).

[4] C. L. Melcher and J. S. Schweitzer, Cerium-doped lutetium orthosilicate: A fast, efficient new scintillator, IEEE Trans. Nucl. Sci. **39**, 502 (1992).

[5] D. W. Cooke, K. J. McClellan, B. L. Bennett, J. M. Roper, M. T. Whittaker, R. E. Muenchausen, and R. C. Sze, Crystal growth and optical characterization of cerium-doped $Lu_{1.8}Y_{0.2}SiO_5$, J. Appl. Phys. **88**, 7360 (2000).

[6] M. Conti, State of the art and challenges of time-of-flight PET, Phys. Med. **25**, 1 (2009).

[7] E. Auffray, B. Frisch, F. Geraci, A. Ghezzi, S. Gundacker, H. Hillemanns, P. Jarron, T. Meyer, M. Paganoni, K. Pauwels, M. Pizzichemi, and P. Lecoq, A comprehensive and systematic study of coincidence time resolution and light yield using scintillators of different size, wrapping and doping, IEEE Nucl. Sci. Symp. Conf. Rec. **N4-6**, 64 (2011).

[8] W. W. Moses, Time of flight in PET revisited, IEEE Trans. Nucl. Sci. **50**, 1325 (2003).

[9] M. A. Spurrier, P. Szupryczynski, K. Yang, A. A. Carey, and C. L. Melcher, Effects of Ca^{2+} co-doping on the scintillation properties of LSO:Ce, IEEE Trans. Nucl. Sci. **55**, 1178 (2008).

[10] S. Blahuta, A. Bessière, B. Viana, P. Dorenbos, and V. Ouspenski, Evidence and consequences of Ce^{4+} in LYSO:Ce, Ca and LYSO:Ce, Mg single crystals for medical imaging applications, IEEE Trans. Nucl. Sci. **60**, 3134 (2013).

[11] S. P. Liu, X. Q. Feng, Z. W. Zhou, M. Nikl, Y. Shi, and Y. B. Pan, Effect of Mg^{2+} co-doping on the scintillation performance of LuAG:Ce ceramics, Phys. Status Solidi RRL **8**, 105 (2014).

[12] M. Nikl, K. Kamada, V. Babin, J. Pejchal, K. Pilarova, E. Mihokova, A. Beitlerova, K. Bartosiewicz, S. Kurosawa, and A. Yoshikawa, Defect engineering in Ce-doped aluminum garnet single crystal scintillators, Cryst. Growth Des. **14**, 4827 (2014).

[13] K. Yang, C. L. Melcher, M. A. Koschan, and M. Zhuravleva, Effect of Ca co-doping on the luminescence centers in LSO:Ce single crystals, IEEE Trans. Nucl. Sci. **58**, 1394 (2011).

[14] M. Koschan, K. Yang, M. Zhuravleva, and C. L. Melcher, A comparison of the effect of Ca^{2+} codoping in cerium doped GSO with that of LSO and YSO, J. Cryst. Growth **352**, 133 (2012).

[15] M. Nikl, J. Pejchal, E. Mihokova, J. A. Mares, H. Ogino, A. Yoshikawa, T. Fukuda, A. Vedda, and C. D'Ambrosio, Antisite defect-free $Lu_3(Ga_xAl_{1-x})_5O_{12}$:Pr scintillator, Appl. Phys. Lett. **88**, 141916 (2006).

[16] M. Fasoli, A. Vedda, M. Nikl, C. Jiang, B. P. Uberuaga, D. A. Andersson, K. J. McClellan, and C. R. Stanek, Band-gap engineering for removing shallow traps in rare-earth $Lu_3Al_5O_{12}$ garnet scintillators using Ga^{3+} doping, Phys. Rev. B **84**, 081102(R) (2011).

[17] Y. T. Wu, J. L. Luo, M. Nikl, and G. H. Ren, Origin of improved scintillation efficiency in $(Lu, Gd)_3(Ga, Al)_5O_{12}$:Ce multicomponent garnets: An X-ray absorption near edge spectroscopy study, APL Mater. **2**, 012101 (2014).

[18] K. Kamada, T. Yanagida, J. Pejchal, M. Nikl, T. Endo, K. Tsutumi, Y. Fujimoto, A. Fukabori, and Y. Yoshikawa, Scintillator-oriented combinatorial search in Ce-doped $(Y, Gd)_3(Ga, Al)_5O_{12}$ multicomponent garnet compounds, J. Phys. D **44**, 505104 (2011).

[19] K. Kamada, T. Endo, K. Tsutumi, T. Yanagida, Y. Fujimoto, A. Fukabori, A. Yoshikawa, J. Pejchal, and M. Nikl, Composition engineering in cerium-doped $(Lu, Gd)_3(Ga, Al)_5O_{12}$ single crystal scintillators, Cryst. Growth Des. **11**, 4484 (2011).

[20] J. A. Mares, M. Nikl, E. Mihokova, A. Beitlerova, A. Vedda, and C. D'Ambrosio, Scintillation response comparison among Ce-doped aluminum garnets, perovskites and orthosilicate, IEEE Trans. Nucl. Sci. **55**, 1142 (2008).

[21] K. Kamada, T. Yanagida, T. Endo, K. Tsutumi, Y. Usuki, M. Nikl, Y. Fujimoto, A. Fukabori, and A. Yoshikawa, 2 inch

diameter single crystal and scintillation properties of $Ce:Gd_3Al_2Ga_3O_{12}$, J. Cryst. Growth **352**, 88 (2012).
[22] M. Tyagi, F. Meng, M. Koschan, S. B. Donnald, H. Rothfuss, and C. L. Melcher, Effects of codoping on scintillation and optical properties of a Ce-doped $Gd_3Ga_3Al_2O_{12}$ scintillator, J. Phys. D **46**, 475302 (2013).
[23] F. Meng, M. Koschan, Y. T. Wu, C. L. Melcher, and P. Cohen, Relationship between Ca^{2+} concentration and properties of GGAG:Ce scintillators, IEEE Trans. Nucl. Sci. (unpublished).
[24] P. Dorenbos, Systematic behavior in trivalent lanthanide charge transfer energies, J. Phys. Condens. Matter **15**, 8417 (2003).
[25] D. Z. Ding, H. Feng, G. H. Ren, M. Nikl, L. S. Qin, S. K. Pan, and F. Yang, Air atmosphere annealing effects on LSO:Ce crystal, IEEE Trans. Nucl. Sci. **57**, 1272 (2010).
[26] B. Ravel and M. Newville, ATHENA and ARTEMIS: Interactive graphical data analysis using IFEFFIT, Phys. Scr. **115**, 1007 (2005).
[27] G. Kresse and J. Hafner, Ab initio molecular dynamics for liquid metals, Phys. Rev. B **47**, 558 (1993).
[28] G. Kresse and D. Joubert, From ultrasoft pseudopotentials to the projector augmented-wave method, Phys. Rev. B **59**, 1758 (1999).
[29] J. P. Perdew, K. Burke, and M. Ernzerhof, Generalized gradient approximation made simple, Phys. Rev. Lett. **77**, 3865 (1996).
[30] S. L. Dudarev, G. A. Botton, S. Y. Savrasov, C. J. Humphreys, and A. P. Sutton, Electron-energy-loss spectra and the structure stability of nickel oxide: An LSDA + U study, Phys. Rev. B **57**, 1505 (1998).
[31] V. I. Anisimov, F. Aryasetiawan, and A. I. Lichtenstein, First-principles calculations of the electronic structure and spectra of strongly correlated systems: The LDA + U method, J. Phys. Condens. Matter **9**, 767 (1997).
[32] Y. N. Xu, W. Y. Ching, and B. K. Brickeen, Electronic structure and bonding in garnet crystals $Gd_3Sc_2Ga_3O_{12}$, $Gd_3Sc_2Al_3O_{12}$, and $Gd_3Ga_5O_{12}$ compared to $Y_3Al_5O_{12}$, Phys. Rev. B **61**, 1817 (2000).
[33] J. P. Perdew, M. Ernzerhof, and K. Burke, Rationale for mixing exact exchange with density functional approximations, J. Chem. Phys. **105**, 9982 (1996).
[34] L. Hedin, New method for calculating the one-particle green's function with application to the electron-gas problem, Phys. Rev. **139**, A796 (1965).
[35] Y. N. Xu and W. Y. Ching, Electronic structure of yttrium aluminum garnet ($Y_3Al_5O_{12}$), Phys. Rev. B **59**, 10530 (1999).
[36] A. Zunger, S.-H. Wei, L. G. Ferreira, and J. E. Bernard, Special quasirandom structures, Phys. Rev. Lett. **65**, 353 (1990).
[37] See Supplemental Materials at http://link.aps.org/supplemental/10.1103/PhysRevApplied.2.044009 for crystal data and structure refinement for $Gd_3Ga_3Al_2O_{12}$.
[38] Y. T. Wu, M. Nikl, V. Jary, and G. H. Ren, Thermally induced ionization of $5d_1$ state of Ce^{3+} ion in $Gd_3Ga_3Al_2O_{12}$ host, Chem. Phys. Lett. **574**, 56 (2013).
[39] W. Chewpraditkul, C. Wanarak, T. Szczesniak, M. Moszynski, V. Jary, A. Beitlerova, and M. Nikl, Opt. Mater. **35**, 1679 (2013).
[40] J. A. Dean, *Lange's Handbook of Chemistry*, 15th ed. (McGraw-Hill, New York, 1979).
[41] C. Mansuy, J. M. Nedelec, and R. Mahiou, Molecular design of inorganic scintillators: From alkoxides to scintillating materials, J. Mater. Chem. **14**, 3274 (2004).
[42] C. L. Melcher, S. Friedrich, S. P. Cramer, M. A. Spurrier, P. Szupryczynski, and R. Nutt, Cerium oxidation state in LSO:Ce scintillators, IEEE Trans. Nucl. Sci. **52**, 1809 (2005).
[43] M. Fasoli, A. Vedda, A. Lauria, F. Moretti, E. Rizzelli, N. Chiodini, F. Meinardi, and M. Nikl, Effect of reducing sintering atmosphere on Ce-doped sol-gel silica glasses, J. Non-Cryst. Solids **355**, 1140 (2009).
[44] C. R. Stanek, C. Jiang, S. K. Yadav, K. J. McClellan, B. P. Uberuaga, D. A. Andersson, and M. Nikl, The effect of Ga-doping on the defect chemistry of $RE_3Al_5O_{12}$ garnets, Phys. Status Solidi (b) **250**, 244 (2013).
[45] P. Dorenbos, Electronic structure and optical properties of the lanthanide activated $RE_3(Al_{1-x}Ga_x)_5O_{12}$ (RE = Gd, Y, Lu) garnet compounds, J. Lumin. **134**, 310 (2013).
[46] A. Belén Muñoz-García and L. Seijo, Structural, electronic, and spectroscopic effects of Ga codoping on Ce-doped yttrium aluminum garnet: First-principles study, Phys. Rev. B **82**, 184118 (2010).
[47] Y. Zorenko, T. Zorenko, and T. Voznyak, Luminescence centers in $Y_3Al_5O_{12}:La$ single crystals, *J. Phys. Conf. Ser.* 289, 012028 (2011).
[48] V. Babin, V. V. Laguta, A. Maaroos, A. Makhov, M. Nikl, and S. Zazubovich, Luminescence of F^+-type centers in undoped $Lu_3Al_5O_{12}$ single crystals, Phys. Status Solidi (b) **248**, 239 (2011).
[49] L. Guerbous and O. Krachni, Luminescence of Ce^{3+} traces in Pr^{3+}-doped $LuBO_3$ and YBO_3 orthoborates, Radiat. Eff. Defects Solids **161**, 199 (2006).
[50] P. A. Tanner, C. S. K. Mak, N. M. Edelstein, K. M. Murdoch, G. Liu, J. Huang, L. Seijo, and Z. Barandiarán, Absorption and emission spectra of Ce^{3+} in elpasolite lattices, J. Am. Chem. Soc. **125**, 13225 (2003).
[51] L. Van Pieterson, S. Soverna, and A. Meijerink, On the nature of the luminescence of Sr_2CeO_4, J. Electrochem. Soc. **147**, 4688 (2000).
[52] L. Li, S. Zhou, and S. Zhang, Investigation on charge transfer of Ce^{4+} in Sr_2CeO_4 blue phosphor, Chem. Phys. Lett. **453**, 283 (2008).
[53] S. R. Rotman, H. L. Tuller, and C. Warde, Defect-property correlations in garnet crystals. VI. The electrical conductivity, defect structure, and optical properties of luminescent calcium and cerium-doped yttrium aluminate garnet, J. Appl. Phys. **71**, 1209 (1992).
[54] B. Liu, C. S. Shi, Y. G. Wei, and J. Y. Liao, the traps effect on temperature dependence of luminescence from $PbWO_4$ crystals, Chem. Phys. Lett. **362**, 296 (2002).
[55] A. J. Wojtowicz, A. Lempicki, D. Wisniewski, M. Balcerzyk, and C. Brecher, The carrier capture and recombination processes in Ln^{3+}-activated scintillators, IEEE Trans. Nucl. Sci. **43**, 2168 (1996).

[56] V. Babin, K. Blazek, A. Krasnikov, K. Nejezchleb, M. Nikl, T. Savikhina, and S. Zazubovich, Luminescence of undoped LuAG and YAG crystals, Phys. Status Solidi (c) **2**, 97 (2005).

[57] M. Kirm, A. Lushchik, Ch. Lushchik, and G. Zimmerer, in *Physics and Chemistry of Luminescent Materials*, edited by C. Ronda *et al.*, The Electrochem. Soc. Proc. Ser. PV 99–40 (The Electrochemical Society, Pennington, NJ, 2000), pp. 113–122.

[58] D. S. Hamilton, S. K. Gayen, G. J. Pogatshnik, R. D. Ghen, and W. J. Miniscalco, Optical-absorption and photo-ionization measurements from the excited states of $Ce^{3+}:Y_3Al_5O_{12}$, Phys. Rev. B **39**, 8807 (1989).

[59] B. Ferrand, B. Viana, L. Pidol, and P. Dorenbos, Low-delayed luminescence dense and rapid scintillator material, U.S. Patent No. 7,651,632 B2 (26 January 2010).

[60] B. Ferrand, B. Viana, L. Pidol, and P. Dorenbos, Dense high-speed scintillator material of low afterglow, U.S. Patent No. 8,034,258 B2 (11 October 2011).

[61] H. Feng, V. Jary, E. Mihokova, D. Z. Ding, M. Nikl, G. H. Ren, H. Y. Li, S. K. Pan, A. Beitlerova, and R. Kucerkova, Temperature dependence of luminescence characteristics of $Lu_{2(1-x)}Y_{2x}SiO_5:Ce^{3+}$ scintillator grown by the Czochralski method, J. Appl. Phys. **108**, 033519 (2010).